ROYAL SOCIETY
OF CHEMISTRY

Check for updates

Hollow Ru/RuO₂ nanospheres with nanoparticulate shells for high performance electrocatalytic oxygen evolution reactions†

Kyoungil Cho, ‡[a] June Young Jang,‡[a] Yoon-Joo Ko,[b] Yoon Myung*[c] and Seung Uk Son *[a]

This work shows that hollow Ru/RuO₂ nanoparticles having nanoparticulate shells (HN-Ru/RuO₂) can be prepared using hollow microporous organic polymers with Ru species (H-MOP-Ru) as precursors. Using silica spheres as templates, H-MOPs were prepared through the Sonogashira–Hagihara coupling of 1,3,5-triethynylbenzene with 2,3-ethoxymethylenedioxy-1,4-diiodobenzene. Acid hydrolysis of cyclic ethyl orthoformate protecting groups generated catechol moieties to form H-MOP-Cat. Then, H-MOP-Ru was obtained by incorporating Ru species into H-MOP-Cat. Heat-treatment of H-MOP-Ru under air induced the formation of HN-Ru/RuO₂ with a diameter of 61 nm and shells consisting of 6–7 nm nanoparticles. Due to the hollow structure and nanoparticulate shells, HN-Ru/RuO₂ showed a high surface area of 80 m² g⁻¹ and a pore volume of 0.18 cm³ g⁻¹. The HN-Ru/RuO₂ showed enhanced electrocatalytic performance for the oxygen evolution reaction (OER) with an overpotential of 295 mV @ 10 mA cm⁻² and a Tafel slope of 46 mV dec⁻¹ in alkaline electrolyte, compared with control RuO₂ such as commercial Ru/RuO₂ nanoparticles (A-Ru/RuO₂) and home-made Ru/RuO₂ nanoparticles (N-Ru/RuO₂) prepared *via* the same synthetic procedure as HN-Ru/RuO₂. While HN-Ru/RuO₂ inevitably contained Pd originated from coupling catalysts, it showed superior performance to Ru/RuO₂ nanoparticles with the same Pd content (N1-Ru/RuO₂), indicating that the efficient electrocatalytic performance of HN-Ru/RuO₂ is attributable to its hollow structure and nanoparticulate shells.

Introduction

As climate change is becoming a more and more critical issue in our society, carbon neutralization-related technologies are attracting great attention from scientists.[1] Hydrogen has been considered as an alternative energy source of carbon-based fossil fuels.[2] To realize the hydrogen economy, the production, storage, and utilization technologies of hydrogen require continuous advances.[2] For hydrogen production, electrocatalytic water splitting has been regarded as one of the most promising methods.[3] To realize electrocatalytic full water splitting, efficient electrocatalysts for both the cathodic

hydrogen evolution reaction (HER) and anodic oxygen evolution reaction (OER) are required.[3] While significant progress has been made in the development of HER electrocatalysts, OER electrocatalysts require more exploration.[4]

Ru/RuO₂ has been studied as a representative electrocatalyst for the OER.[5] However, the OER process catalyzed by Ru/RuO₂ is

[a] Department of Chemistry, Sungkyunkwan University, Suwon 16419, Korea. E-mail: sson@skku.edu

[b] Laboratory of Nuclear Magnetic Resonance, National Center for Inter University Research Facilities (NCIRF), Seoul National University, Seoul 08826, Korea

[c] Korea Institute of Industrial Technology, Advanced Energy Materials and Components R&D Group, Busan 46744, Korea. E-mail: myungyoon@kitech.re.kr

† Electronic supplementary information (ESI) available: SEM images of MOP and Ru/RuO₂ materials, PXRD patterns of MOP materials, XPS analysis, cyclic voltammograms of Ru/RuO₂ materials, EIS results, table of the physical features of MOP and Ru/RuO₂ materials, and OER performance survey table of RuO₂ materials. See DOI: https://doi.org/10.1039/d3na00899a

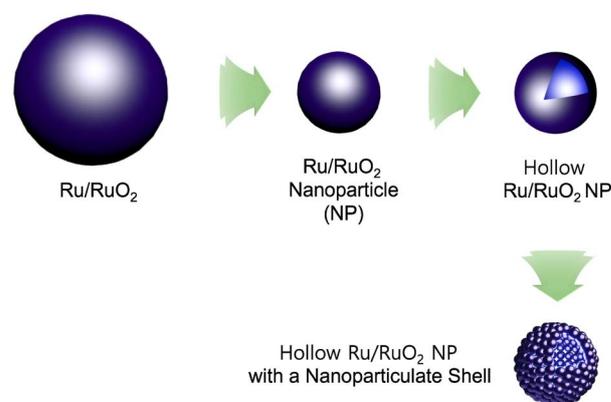‡ These authors contributed equally to this work.

Fig. 1 Morphology engineering of Ru/RuO₂ electrocatalysts to nanoparticles, hollow nanoparticles, and hollow nanoparticles with nanoparticulate shells.

relatively slow. Morphology engineering of Ru/RuO$_2$ can improve its catalytic performance (Fig. 1).[6,7]

For example, nanosized Ru/RuO$_2$ particles showing improved electrocatalytic OER performance, due to enhanced surface area and efficient utilization of catalytic sites, have been prepared.[6–8] Recently, it has been reported that a hollow structure can enhance the catalytic performance of nano-sized catalysts, due to efficient mass transfer of substrates and high surface areas.[9] Moreover, hollow Ru/RuO$_2$ nanoparticles with nanoparticulate shells (HN-Ru/RuO$_2$) can be a promising candidate for development of efficient electrocatalysts for the OER. However, the synthetic route to the HN-Ru/RuO$_2$ is limited, thus requiring further exploration.[10]

Recently, microporous organic polymers (MOPs) have been prepared by various coupling reactions of organic building blocks.[11–15] Moreover, using anchoring groups, metals can be incorporated into MOPs.[16–26] Our research group has reported morphology-engineered synthesis of MOPs.[27] Especially, hollow MOPs (H-MOPs) have been prepared using silica and metal organic framework particles as templates.[28,29] The H-MOPs can be utilized as templates for synthesizing inorganic nano-materials such as hollow Ru/RuO$_2$ nanomaterials.

In this work, we report the synthesis of hollow MOPs bearing catechol moieties (H-MOP-Cat). Incorporation of Ru species into hollow MOPs and successive calcination under air resulted in the formation of hollow Ru/RuO$_2$ nanoparticles. Especially, the shells of hollow Ru/RuO$_2$ nanoparticles have a nanoparticulate feature. The resultant HN-Ru/RuO$_2$ showed excellent OER performance, better than that of Ru/RuO$_2$ nanomaterials.

Experimental

General information

Scanning electron microscopy (SEM) was conducted using a JSM7100F microscope at the Chiral Material Core Facility Center of Sungkyunkwan University. Transmission electron microscopy (TEM) and high-resolution TEM (HR-TEM) images were obtained using a JSM2100F microscope. Energy dispersive X-ray spectroscopy (EDS) was conducted using TEM equipment. N$_2$ adsorption–desorption isotherm curves were obtained at 77 K using a Micromeritics ASAP2020. The surface areas of materials were measured through analysis of adsorption isotherm curves based on Brunauer–Emmett–Teller (BET) theory. Pore size analysis diagrams were obtained through analysis of N$_2$ adsorption curves based on the non-local density functional theory (NLDFT) method. X-ray photoelectron spectroscopy (XPS) was conducted using a Thermo VG spectrometer. Powder X-ray diffraction (PXRD) studies were conducted using a Rigaku MAX-2200. Infrared (IR) absorption spectroscopy was conducted using a Bruker VERTEX70. Solid state ^{13}C nuclear magnetic resonance spectroscopy (NMR) was conducted in cross polarization (CP)/total sideband suppression (TOSS) mode using a 500 MHz Bruker AVANCE II NMR spectrometer. Solution state ^{1}H NMR spectra were obtained using a Bruker Ascend 500 spectrometer. Thermogravimetric analysis (TGA) was conducted using a TG/DTA 7300. Inductively coupled plasma atomic emission spectroscopy (ICP-AES) analysis was conducted using an OPTIMA 8300.

Synthesis of building blocks

To prepare a cyclic ethyl orthoformate-protected 1,4-diiodo-2,3-catechol (2,3-ethoxymethylenedioxy-1,4-diiodobenzene) building block (Fig. 2), 2,3-dihydroxy-1,4-diiodobenzene was synthesized, following the synthetic method reported in the literature.[30,31] In this work, the following procedures were applied. 1,2-Dimethoxybenzene (18.5 mL, 0.145 mol), tetramethylethylenediamine (20 mL, 0.13 mol), and distilled hexane (50 mL) were added to a flame-dried 250 mL Schlenk flask under argon. After n-BuLi (1.6 M in hexane, 100 mL, 0.16 mol) was added dropwise for 1 h, the reaction mixture was stirred at room temperature for 28 h. After trimethylsilyl chloride (22.5 mL, 0.177 mol) was added dropwise at −78 °C, the reaction mixture was stirred at room temperature for 5 h. After further stirring at
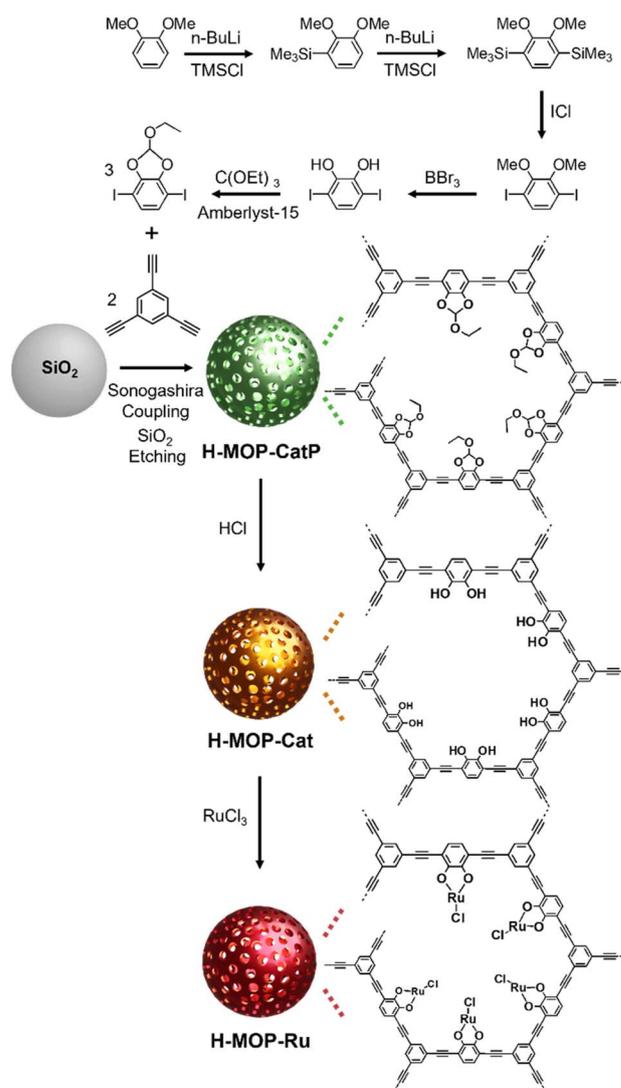

Fig. 2 Synthesis of a cyclic ethyl orthoformate (Ceof)-protected 1,4-diiodo-2,3-catechol (2,3-ethoxymethylenedioxy-1,4-diiodobenzene) building block, H-MOP-CatP, H-MOP-Cat, and H-MOP-Ru.

30 °C for 30 min, the product was extracted using hexane and water. After the hexane solution was dried with $MgSO_4$, the volatile liquid was evaporated. Then 1,2-dimethoxy-3-trimethylsilylbenzene was isolated by flash column chromatography.

To prepare 2,3-dimethoxy-1,4-bis(trimethylsilyl)benzene, 1,2-dimethoxy-3-trimethylsilylbenzene (30.4 g, 0.145 mol), tetramethylethylenediamine (20 mL, 0.13 mol), and distilled hexane (50 mL) were added to a flame-dried 250 mL Schlenk flask under argon. After n-BuLi (1.6 M in hexane, 100 mL, 0.16 mol) was added dropwise for 1 h, the reaction mixture was stirred at room temperature for 28 h. After trimethylsilyl chloride (22.5 mL, 0.177 mol) was added at −78 °C dropwise, the reaction mixture was stirred at room temperature for 5 h. After the reaction mixture was further stirred at 30 °C for 30 min, the product was extracted using hexane and water. After the hexane solution was dried with $MgSO_4$, the volatile liquid was evaporated. Then 2,3-dimethoxy-1,4-bis(trimethylsilyl)benzene was isolated by flash column chromatography.

To prepare 1,4-diiodo-2,3-dimethoxybenzene, 2,3-dimethoxy-1,4-bis(trimethylsilyl)benzene (31 g, 0.11 mol) and distilled methylene chloride (160 mL) were added to a 500 mL round-bottomed flask. After iodine monochloride (44.6 g, 0.275 mol) dissolved in methylene chloride (160 mL) was added dropwise, the reaction mixture was stirred at room temperature for 30 min. Using an aqueous sodium thiosulfate solution, the product was extracted. After drying the methylene chloride solution with $MgSO_4$, the volatile liquid was evaporated to obtain 1,4-diiodo-2,3-dimethoxybenzene. To prepare 2,3-dihydroxy-1,4-diiodobezene, 1,4-diiodo-2,3-dimethoxybenzene (6.0 g, 17 mmol) and methylene chloride (3 mL) were added to a flame-dried 100 mL Schlenk flask under argon. After cooling to −78 °C, BBr_3 (1 M in methylene chloride, 50 mL, 50 mmol) was added dropwise. After its temperature increased to room temperature, the reaction mixture was poured into ice water. The product was extracted using methylene chloride and water. After drying with sodium sulfate, the volatile liquid was evaporated. Then 2,3-dihydroxy-1,4-diiodobezene was purified by flash column chromatography.

To prepare a Ceof-protected 1,4-diiodo-2,3-catechol building block, 2,3-dihydroxy-1,4-diiodobezene (2.4 g, 6.6 mmol) and distilled toluene (65 mL) were added to a flame-dried 250 mL Schlenk flask. After Amberlyst-15 (45 mg) and triethyl orthoformate (3.3 mL, 20 mmol) were added, the reaction mixture was stirred at 140 °C for 18 h. After cooling to room temperature, the volatile liquid was evaporated. After the product was extracted using methylene chloride and water, the methylene chloride solution was dried with $MgSO_4$. After the volatile liquid was evaporated, cyclic ethyl orthoformate-protected 1,4-diiodo-2,3-catechol was isolated by flash column chromatography. The ^1H NMR spectrum of the building block, cyclic ethyl orthoformate-protected 1,4-diiodo-2,3-catechol, matched well with that described in the literature.[30,31]

Synthesis of H-MOP-Ru

To synthesize H-MOP-Ru, H-MOP-CatP (refer to Fig. 2) was prepared as follows. To use as templates, silica spheres with an average diameter of 180 nm were prepared by the Stöber method reported in the literature.[32] In this work, the following procedures were applied. Aqueous ammonia solution (25–30%, 5 mL), water (8 mL), and ethanol (200 mL) were added to a 250 mL round-bottomed flask. After stirring at room temperature for 30 min, tetraethyl orthosilicate (TEOS, 14 mL) was added. The reaction mixture was stirred at room temperature for 18 h. After a mixture of methylene chloride (30 mL) and hexane (200 mL) was added to the reaction mixture, silica spheres were isolated by centrifugation, washed with a mixture of methanol (20 mL) and acetone (20 mL) four times, and dried under vacuum.

Silica spheres (0.30 g), $(PPh_3)_2PdCl_2$ (14 mg, 20 μmol), CuI (4.0 mg, 20 μmol), distilled triethylamine (TEA, 40 mL), distilled tetrahydrofuran (THF, 12 mL), and distilled dimethylformamide (DMF, 3 mL) were added to a flame-dried Schlenk flask under argon. After the reaction mixture was sonicated at room temperature for 1 h, the THF solution (5 mL) of 2,3-ethoxymethylenedioxy-1,4-diiodobenzene (0.12 g, 0.30 mmol) and 1,3,5-triethynylbenzene (30 mg, 0.20 mmol) was added at room temperature. The reaction mixture was stirred at 80 °C for 24 h. After cooling to room temperature, SiO_2@MOP-CatP was separated by centrifugation, washed with a mixture of methylene chloride (15 mL) and acetone (25 mL) three times and methanol (40 mL) three times, and dried under vacuum. After SiO_2@MOP-CatP was added to a 50 mL Falcon tube, a mixture of hydrofluoric acid (48%, 5 mL), THF (10 mL), and water (15 mL) was added. Caution: Since hydrofluoric acid solution is extremely toxic, it should be handed with specific gloves in an effective hood. After stirring at room temperature for 2 h, the H-MOP-CatP was isolated by centrifugation, washed with a mixture of methanol (10 mL) and water (30 mL) five times, methanol (40 mL) two times, and acetone (40 mL) once, and dried under vacuum.

To prepare H-MOP-Cat, H-MOP-CatP (0.15 g) and THF (40 mL) were added to a 100 mL Schlenk flask. After cooling to 0 °C, hydrochloric acid (21 mL) was added to the reaction mixture. After stirring at room temperature for 24 h, H-MOP-Cat was isolated from the reaction mixture by centrifugation, washed with a mixture of water (30 mL) and methanol (10 mL) five times, methanol (40 mL) two times, and acetone (40 mL) once, and dried under vacuum. To prepare H-MOP-Ru, H-MOP-Cat (50 mg), $RuCl_3 \cdot 3H_2O$ (0.10 g, 0.38 mmol), and distilled methanol (15 mL) were added to a 50 mL Schlenk flask under argon. The reaction mixture was stirred at 80 °C for 24 h. After cooling to room temperature, the H-MOP-Ru was isolated by centrifugation, washed with methanol (40 mL) once, and dried under vacuum.

Synthesis of HN-Ru/RuO₂ and control Ru/RuO₂ materials (A-Ru/RuO₂, N-Ru/RuO₂, and N1-Ru/RuO₂)

To prepare $HN-Ru/RuO_2$, the precursor material, H-MOP-Ru, was heated at 500 °C for 4 h under air in a muffle furnace (CT-DMF3, Coretech Co.). As a control material, commercial Ru/RuO_2 nanoparticles were purchased from Aldrich Chem. Co (Cat. no. 238058). Another control material, N-Ru/RuO_2, was

obtained by heating $RuCl_3 \cdot 3H_2O$ at 500 °C for 4 h under air. N1-Ru/RuO_2 was obtained by heating a mixture of $RuCl_3 \cdot 3H_2O$ (0.30 g, 1.1 mmol) and $(PPh_3)_2PdCl_2$ (0.23 g, 0.33 mmol) at 500 °C for 4 h under air.

Electrochemical studies for the OER

Electrochemical studies were conducted using a three-electrode cell connected to an electrochemical analyzer (Biologic, EC-LAB Co.). Ag/AgCl (saturated with 3 M KCl, Aldrich Chemical Co.) and a graphite rod with a diameter of 6 mm and a length of 102 mm (Pine, 99.9995%) were used as a reference electrode and a counter electrode, respectively. 1.0 M KOH solution was used as an electrolyte. Working electrodes were fabricated as follows. Ru/RuO_2 catalysts (5 mg) were well dispersed in a mixture of Nafion solution (5%, 20 μL) and isopropyl alcohol (0.98 mL) through sonication. The resultant slurry ink (20 μL) was loaded on a glassy carbon rotating electrode (RDE, area of 0.164 cm^2, Pine). The loading amount of Ru/RuO_2 catalysts was calculated to be 0.61 mg cm^{-2}. The electrocatalytic performance of Ru/RuO_2 materials for the OER was investigated through linear sweep voltammetry with iR correction, a scan rate of 5 mV s^{-1}, and a rotation speed of 1600 rpm at room temperature. The 1.0 M KOH electrolyte was purged with O_2 gas during measurements. Applied potentials (E) reported in this work were referenced to the reversible hydrogen electrode (RHE) through standard calibration with the following equation: E (vs. RHE) = E (vs. Ag/AgCl) + $E_{Ag/AgCl}$ (= 0.197 V) + 0.0592 pH = E (vs. Ag/AgCl) + 1.0258 V.

Results and discussion

Fig. 2 shows a synthetic scheme for hollow MOPs with cyclic ethyl orthoformate-protected catechol moieties (H-MOP-CatP), H-MOP-Cat, hollow MOPs with Ru-catecholates (H-MOP-Ru), and a building block. To synthesize H-MOP-CatP, we prepared a cyclic ethyl orthoformate-protected 1,4-diiodo-2,3-catechol (2,3-ethoxymethylenedioxy-1,4-diiodobenzene) building block from 1,2-dimethoxybenzene (Fig. 2 and refer to the Experimental section for detailed procedures).[30,31] After trimethylsilyl (TMS) groups were introduced to the neighboring sites of methoxy groups of 1,2-dimethoxybenzene, treatment with iodine monochloride resulted in the formation of 1,4-diiodo-2,3-dihydroxybenzene. Unfortunately, direct use of 1,4-diiodo-2,3-dihydroxybenzene as a building block for preparing H-MOP-Cat was unsuccessful, due to quenching of coupling catalysts by catechol groups. Thus, we protected catechol moieties with cyclic ethyl orthoformate (Ceof) groups to form a 2,3-ethoxymethylenedioxy-1,4-diiodobenzene building block.[30,31] Using silica spheres as templates, H-MOP-CatP was obtained through the Sonogashira–Hagihara coupling of 1,3,5-triethynylbenzene and 1.5 eq. of 2,3-ethoxymethylenedioxy-1,4-diiodobenzene and successive silica etching by treatment with aqueous HF solution. Acid-catalyzed hydrolysis of Ceof protecting groups in the H-MOP-CatP resulted in the formation of H-MOP-Cat. Ru species were then incorporated into H-MOP-Cat through treatment with $RuCl_3$ trihydrate to form H-MOP-Ru.
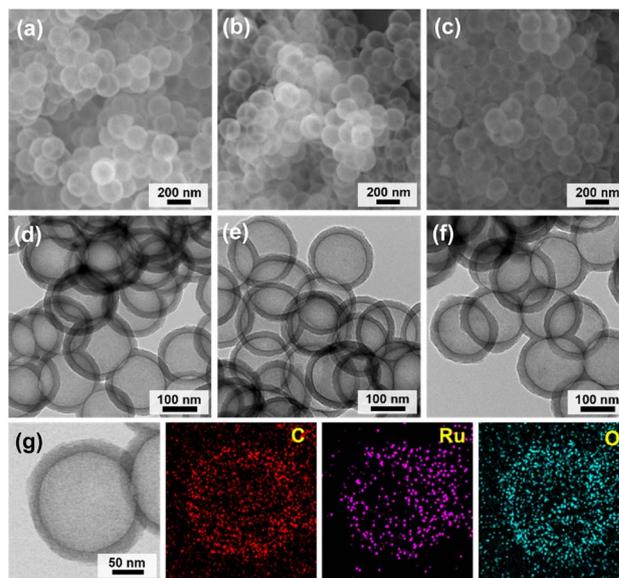

Fig. 3 SEM and TEM images of (a and d) H-MOP-CatP, (b and e) H-MOP-Cat, and (c and f) H-MOP-Ru. (g) EDS-based elemental mapping images of H-MOP-Ru.

The morphologies of H-MOP-CatP, H-MOP-Cat, and H-MOP-Ru were investigated using SEM and TEM analysis (Fig. 3 and S1 in the ESI†). The SEM and TEM images of H-MOP-CatP showed hollow spheres with an average diameter of 195 nm and an average shell thickness of 22 nm (Fig. 3a and d). After hydrolysis of Ceof protecting groups in H-MOP-CatP and Ru coordination to catechol moieties in H-MOP-Cat, the resultant H-MOP-Cat and H-MOP-Ru retained their original hollow morphologies (Fig. 3b, c, e, and f). EDS-based elemental mapping analysis of H-MOP-Ru showed incorporation of Ru into H-MOP-Cat (Fig. 3g).

The surface area and microporosity of the materials were characterized by analyzing N_2 adsorption–desorption isotherm curves based on BET theory and the NL-DFT method (Fig. 4a and b and Table S1 in the ESI†). The surface area and micropore volume (V_{mic}) of H-MOP-CatP were measured to be 399 m^2 g^{-1} and 0.088 cm^3 g^{-1}, respectively. Interestingly, the surface area and V_{mic} of H-MOP-Cat increased significantly to 569 m^2 g^{-1} and 0.14 cm^3 g^{-1}, respectively, indicating successful deprotection of Ceof groups. Ru coordination to H-MOP-Cat induced a decrease of the surface area and V_{mic} of H-MOP-Ru to 361 m^2 g^{-1} and 0.087 cm^3 g^{-1}, respectively. PXRD studies indicated that H-MOP-CatP, H-MOP-Cat, and H-MOP-Ru are amorphous (Fig. S2 in the ESI†).

The chemical structures of the materials were characterized by IR, XPS, and solid state ^{13}C NMR studies (Fig. 4c–e). While the IR spectrum of H-MOP-CatP showed C-O vibration peaks of Ceof groups at 1081 cm^{-1}, H-MOP-Cat showed a decrease of C–O vibrations and appearance of O-H vibrations at 3515 cm^{-1}, due to the generation of catechol moieties.[33–35] Ru coordination induced a shift of C=C vibration peaks from 1581 cm^{-1} (H-MOP-Cat) to 1601–1623 cm^{-1} (H-MOP-Ru). XPS analysis of H-MOP-Ru showed Ru $3p_{1/2}$ and $3p_{3/2}$ orbital peaks at 484.6 and
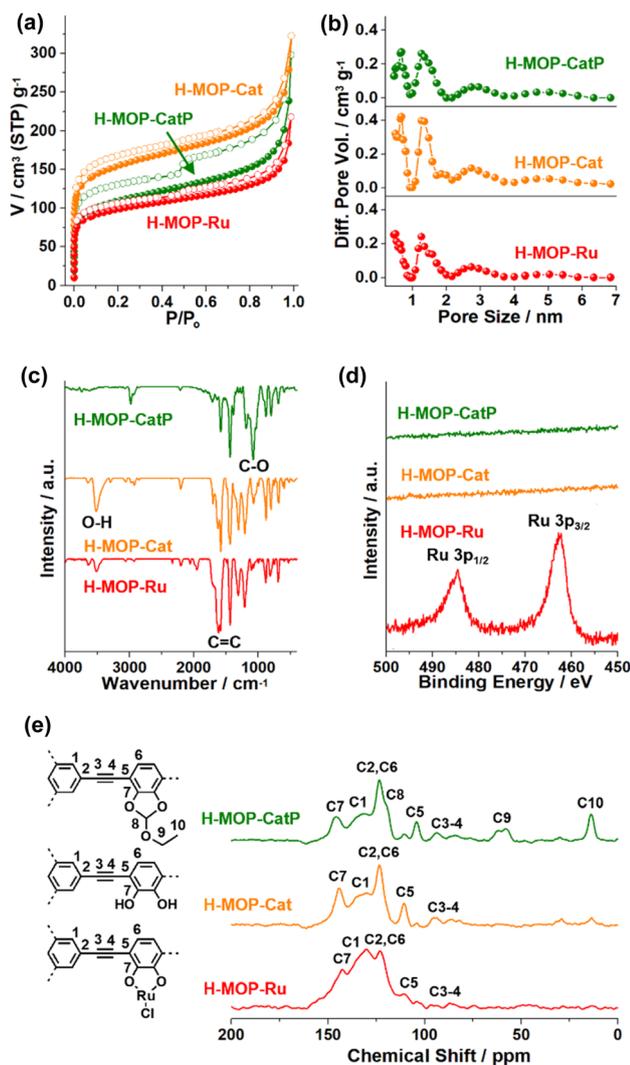
Fig. 4 (a) N_2 sorption isotherm curves obtained at 77 K, (b) pore size distribution diagrams obtained by the NLDFT method, (c) IR absorption spectra, (d) XPS Ru 3p orbitals spectra, and (e) solid state ^{13}C NMR spectra of H-MOP-CatP, H-MOP-Cat, and H-MOP-Ru.

Fig. 5 Synthesis of HN-Ru/RuO_2 and control materials (A-Ru/RuO_2, N-Ru/RuO_2, and N1-Ru/RuO_2).

trihydrate at 500 °C for 4 h under air. Considering the existence of Pd in HN-Ru/RuO_2, originating from the Pd catalyst used in the synthesis of the MOP, we prepared N1-Ru/RuO_2 by the heat treatment of a mixture of $RuCl_3$ trihydrate and $(PPh_3)_2PdCl_2$ at 500 °C for 4 h under air. To match with the content of Pd in HN-Ru/RuO_2, we systematically scanned the amount of $(PPh_3)_2$-$PdCl_2$ for the synthesis of N1-Ru/RuO_2 (refer to the Experimental section for the amounts of Ru and Pd precursors).

SEM and TEM analysis of HN-Ru/RuO_2 showed hollow nanoparticles with an average diameter of 61 nm (Fig. 6a and b). Interestingly, the shells of HN-Ru/RuO_2 consisted of nanoparticles with sizes of 6–7 nm (Fig. 6b). Considering the diameter (195 nm) and shell thickness (22 nm) of the precursor material (H-MOP-Ru), the reduced sizes of HN-Ru/RuO_2 imply significant shrinkage of hollow MOP materials to HN-Ru/RuO_2, due to the combustion-induced removal of carbon. HR-TEM analysis of HN-Ru/RuO_2 clearly confirmed that hollow shells consist of small nanoparticles (Fig. 6c). The (110) and (200) crystalline planes of rutile RuO_2 were exclusively observed in the HR-TEM images of HN-Ru/RuO_2 with inter-crystalline plane distances of 0.32 and 0.23 nm, respectively (Fig. 6c).

The SEM and TEM images of commercial A-Ru/RuO_2 showed spherical nanoparticles with a relatively broad size distribution in the range of 25–70 nm (Fig. 6d and g). In comparison, the SEM and TEM images of N-Ru/RuO_2 showed short rod-like nanomaterials with sizes of ~35 nm × 75 nm (Fig. 6e and h). N1-Ru/RuO_2 also showed irregular granules with a broad size distribution in the range of 7–75 nm (Fig. 6f and i). EDS-based elemental mapping images of HN-Ru/RuO_2 indicated a homogeneous distribution of Ru and O over the materials (Fig. 6j). Interestingly, due to the hollow structural nature of HN-Ru/ RuO_2, its bulk density was much lower than those of A-Ru/RuO_2, N-Ru/RuO_2, and N1-Ru/RuO_2 (refer to Fig. 6k–n showing 40 mg powder in each vial).

Fig. 7 shows the physical and chemical features of Ru/RuO_2 materials. HN-Ru/RuO_2 showed a high surface area of 80 m^2 g^{-1} and mesoporosity with a total pore volume (V_t) of 0.18 cm^3 g^{-1},

462.5 eV, respectively, confirming the formation of Ru(III)–Cl species (Fig. 4d).[36]

The ^{13}C NMR spectrum of H-MOP-CatP showed ^{13}C peaks of Ceof groups at 13.5, 60.2, and 119.6 ppm, in addition to aromatic peaks at 104.3, 123.4, 132.9, and 146.0 ppm and alkyne peaks at 85.0–93.6 ppm (Fig. 4e). In the ^{13}C NMR spectrum of H-MOP-Cat, Ceof groups disappeared, indicating successful deprotection of Ceof groups. H-MOP-Ru showed significant changes of aromatic peaks at 110.5–142.6 ppm, due to Ru coordination to catechol moieties.

TGA curves indicated that H-MOP-Ru is thermally stable up to 275 °C (Fig. S3 in the ESI†). Using H-MOP-Ru as a precursor material, HN-Ru/RuO_2 was obtained by heat-treatment at 500 °C for 4 h under air (Fig. 5). As a control material, commercial Ru/ RuO_2 nanopowders (A-Ru/RuO_2, Aldrich Chem Co., Cat. no. 238058) were obtained. In addition, control Ru/RuO_2 nanoparticles (N-Ru/RuO_2) were prepared by heat-treatment of $RuCl_3$
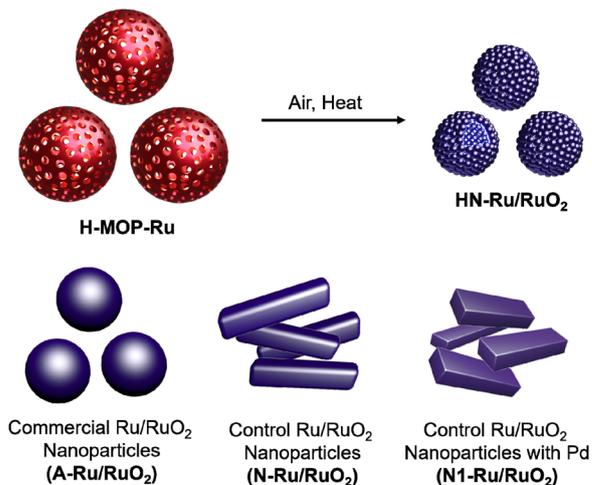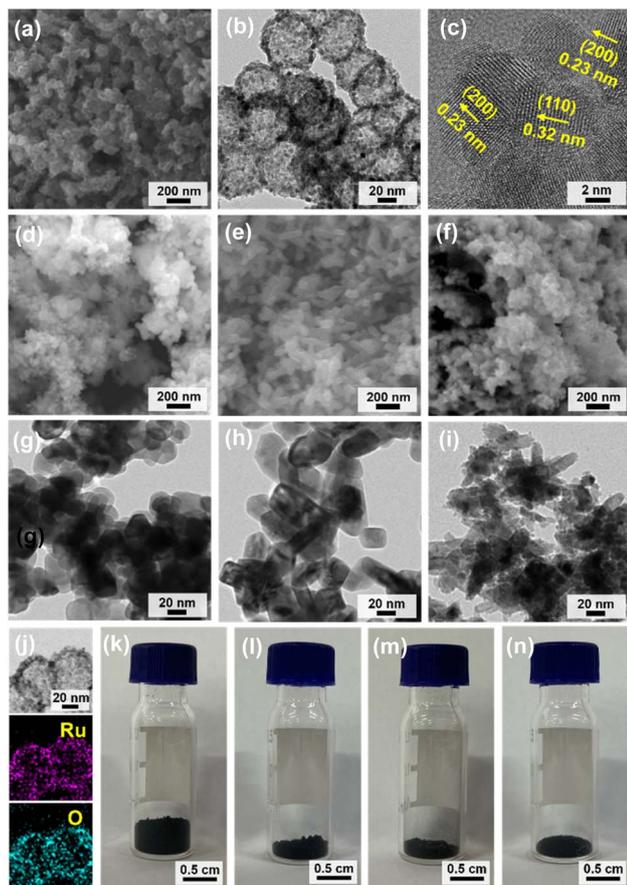
Fig. 6 SEM and TEM images of (a and b) HN-Ru/RuO$_2$, (d and g) A-Ru/RuO$_2$, (e and h) N-Ru/RuO$_2$, and (f and i) N1-Ru/RuO$_2$. (c) HR-TEM and (j) EDS-elemental mapping images of HN-Ru/RuO$_2$. Photographs of (k) HN-Ru/RuO$_2$, (l) A-Ru/RuO$_2$, (m) N-Ru/RuO$_2$, and (n) N1-Ru/RuO$_2$ powders (40 mg powder in each vial).

due to its nanoparticulate shells and hollow structure (Fig. 7a and b and Table S1 in the ESI†). In comparison, A-Ru/RuO$_2$, N-Ru/RuO$_2$, and N1-Ru/RuO$_2$ showed relatively lower surface areas of 10, 6, and 11 m^2 g^{-1} and poor porosity with V_t of 0.019, 0.010, and 0.031 cm^3 g^{-1}, respectively. The PXRD pattern of HN-Ru/RuO$_2$ showed diffraction peaks at 28.1, 35.1, 40.0, and 54.5° (2θ), corresponding to the (110), (101), (200), and (211) crystalline planes of rutile RuO$_2$ (JCPDS# 40-1290), respectively (Fig. 7c). While A-Ru/RuO$_2$, N-Ru/RuO$_2$, and N1-Ru/RuO$_2$ also indicated rutile RuO$_2$, interestingly, all Ru/RuO$_2$ materials showed additional metallic Ru peaks (JCPDS# 65-1863) at 38.3, 41.9, and 43.9° (2θ).

The chemical structures of Ru/RuO$_2$ materials were characterized by XPS studies (Fig. 7d–f and S4 in the ESI†). The Ru 3p$_{1/2}$ and 3p$_{3/2}$ orbital peaks of HN-Ru/RuO$_2$ indicated a mixture of Ru(IV) at 485.7 and 464.1 eV and zerovalent Ru at 483.6 and 461.5 eV, respectively (Fig. 7d).[37] The O 1s orbital peaks of HN-Ru/RuO$_2$ were observed at 528.9 and 530.0 eV, corresponding to inner and surface oxides of RuO$_2$, respectively, in addition to a Pd 3p$_{3/2}$ orbital peak at 531.9 eV (Fig. 7e).[38] According to ICP analysis, the molar ratio of Ru and Pd in HN-Ru/RuO$_2$ was measured to be 83 : 17. The corresponding Pd 3d$_{3/2}$ and 3d$_{5/2}$
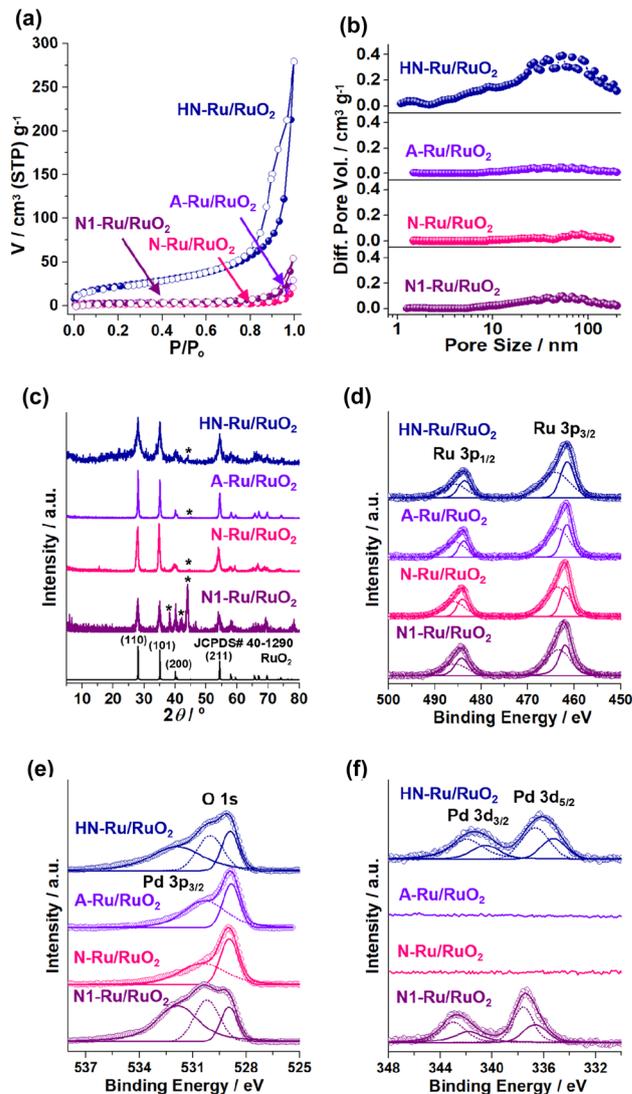

Fig. 7 (a) N$_2$ adsorption−desorption isotherm curves obtained at 77 K, (b) pore size distribution diagrams based on the NLDFT method, (c) PXRD patterns, and (d–f) XPS Ru 3p, O 1s, and Pd 3d orbital spectra of HN-Ru/RuO$_2$, A-Ru/RuO$_2$, N-Ru/RuO$_2$, and N1-Ru/RuO$_2$. The diffraction peaks indicated by asterisks in (c) correspond to metallic Ru (JCSPDS# 65-1863).

orbital peaks of HN-Ru/RuO$_2$ were observed at 341.4 and 336.2 eV, respectively, indicating main PdO species (Fig. 7f).[39]

While the Ru 3p$_{1/2}$ and 3p$_{3/2}$ orbital peaks of A-Ru/RuO$_2$ showed a mixture of Ru(IV) at 485.7 and 463.6 eV and zerovalent Ru at 483.8 and 461.6 eV, the O 1s orbital peaks appeared at 528.8 and 530.3 eV (Fig. 7d and e). Similarly, while the Ru 3p$_{1/2}$ and 3p$_{3/2}$ orbital peaks of N-Ru/RuO$_2$ indicated a mixture of Ru(IV) at 486.0 and 463.6 eV and zerovalent Ru at 484.1 and 461.8 eV, the O 1s orbital peaks were observed at 528.9 and 530.4 eV (Fig. 7d and e).

In the XPS spectrum of N1-Ru/RuO$_2$, the Ru 3p$_{1/2}$ and 3p$_{3/2}$ orbital peaks of Ru(IV) were observed at 485.7 and 463.4 eV, respectively, in addition to zerovalent Ru species at 484.2 and 461.9 eV.[36,37] Similar to those of HN-Ru/RuO$_2$, two O 1s orbital peaks of N1-Ru/RuO$_2$ were observed at 529.0 and 530.2 eV, in

addition to the Pd $3p_{3/2}$ orbital peak at 531.9 eV (Fig. 7d and e).[38] The molar ratio of Ru and Pd of N1-Ru/RuO$_2$ was analyzed to be 82 : 18 by ICP analysis, which was adjusted as a control material of HN-Ru/RuO$_2$ through systematic amount scanning of Pd precursors. The Pd $3d_{3/2}$ and Pd $3d_{5/2}$ orbital peaks of N1-Ru/RuO$_2$ were observed at 342.7 and 337.4 eV, respectively, indicating that the main Pd species is PdO$_2$ (Fig. 7f).[39]

Next, the electrocatalytic performance of the Ru/RuO$_2$ materials for the OER was studied by linear sweep voltammetry using three-electrode electrochemical cells (Fig. 8). When acidic electrolyte was used, the OER activities of Ru/RuO$_2$ materials were not stable, due to their facilitated dissolution.[40–42] Thus, we focused on the OER performance in basic electrolyte (1.0 M KOH). During measurements, the electrolyte was purged with O$_2$ gas. Fig. 8a shows the OER polarization curves when the OER is

Fig. 8 Electrocatalytic performance of HN-Ru/RuO$_2$, A-Ru/RuO$_2$, N-Ru/RuO$_2$, and N1-Ru/RuO$_2$ for the OER in 1.0 M KOH: (a) OER polarization curves, (b) overpotentials at 10 mA cm^{-2}, (c) Tafel plots, (d–e) scan rate dependent cyclic voltammograms (refer to the cyclic voltammograms in Fig. S5 in the ESI† for other control materials) and calculated capacitances, and (f) durability tests measured with potentiometry at a current density of 10 mA cm^{-2}.

electrochemically catalyzed by Ru/RuO$_2$ materials, indicating that HN-Ru/RuO$_2$ revealed OER activity at significantly lower potential (vs. RHE) than A-Ru/RuO$_2$, N-Ru/RuO$_2$, and N1-Ru/RuO$_2$.

While the overpotential @ 10 mA cm^{-2} (η_{10}) of HN-Ru/RuO$_2$ was measured to be 295 mV, those of A-Ru/RuO$_2$, N-Ru/RuO$_2$, and N1-Ru/RuO$_2$ were analyzed to be 345, 355, and 356 mV, respectively (Fig. 8b). Comparing the electrocatalytic performance of HN-Ru/RuO$_2$ with that of N1-Ru/RuO$_2$ or comparing the OER activity of N-Ru/RuO$_2$ with that of N1-Ru/RuO$_2$, it can be speculated that the effect of Pd in HN-Ru/RuO$_2$ and N1-Ru/RuO$_2$ is not significant for the observed performance parameters of electrocatalytic OER, indicating that the hollow and nanoparticulate feature of HN-Ru/RuO$_2$ induced beneficial electrocatalytic performance. It has been reported that in alkaline electrolyte, OH$^-$ is oxidized to oxygen and water through the electrocatalytic OER process.[43] Thus, the effective coordination of *OOH and *OH toward RuO$_2$ electrocatalysts is critical for the high activity toward the OER.[43] Moreover, it has been reported that while the bare surface of RuO$_2$ is inert for electrocatalytic OER, defective surface oxides are actually active.[43] Thus, considering all of this, we suggest that the superior electrocatalytic performance of HN-Ru/RuO$_2$ is attributable to an enhanced defective surface effect of HN-Ru/RuO$_2$, originating from the hollow structure and nanoparticulate shells.

Fig. 8c shows Tafel plots with Tafel slopes of 46, 62, 61, and 71 mV dec^{-1} for HN-Ru/RuO$_2$, A-Ru/RuO$_2$, N-Ru/RuO$_2$, and N1-Ru/RuO$_2$, respectively. The much smaller Tafel slope of HN-Ru/RuO$_2$ than those of A-Ru/RuO$_2$, N-Ru/RuO$_2$, and N1-Ru/RuO$_2$ indicates its faster electrocatalytic OER process.[43] The turnover frequency (TOF) of HN-Ru/RuO$_2$ was calculated to be 0.86 s^{-1} @ 0.30 V, much faster that those (0.15–0.20 s^{-1} @ 0.30 V) of control Ru/RuO$_2$ materials. We suggest that the faster electrocatalytic performance of HN-Ru/RuO$_2$ resulted from the enhanced surface area, due to its hollow structure and nanoparticulate shells.

Fig. 8d–e show the scan-rate dependent cyclic voltammograms (refer to Fig. S5 in the ESI† for cyclic voltammograms of the electrocatalytic OER process by A-Ru/RuO$_2$, N-Ru/RuO$_2$, and N1-Ru/RuO$_2$), indicating that HN-Ru/RuO$_2$ revealed much higher capacitances (C_{dl}: 61 mF cm^{-2}) than control Ru/RuO$_2$ materials (C_{dl}: 1.33–1.43 mF cm^{-2}). The corresponding electrochemical active surface area (ECSA: C_{dl}/C_s, C_{dl} with an area of 0.164 cm^2, C_s: 0.040 mF cm^{-2}) of HN-Ru/RuO$_2$ was calculated to be 2.5 × 10^2 cm^2, much higher than the 5.9–5.5 cm^2 of the control Ru/RuO$_2$ materials. According to electrochemical impedance spectroscopy (EIS), the charge transfer resistance (R_{ct}: 29.2 Ω) of HN-Ru/RuO$_2$ was significantly lower than those of A-Ru/RuO$_2$ (39.3 Ω), N-Ru/RuO$_2$ (45.5 Ω), and N1-Ru/RuO$_2$ (47.5 Ω), indicating the effective interaction of HN-Ru/RuO$_2$ with substrates (Fig. S6 in the ESI†).

Finally, the durability of HN-Ru/RuO$_2$ was studied with potentiometry for overpotentials at 10 mA cm^{-2}, revealing >98% retention of the original electrocatalytic performance for the OER during 12 h (Fig. 8f). After the durability test, TEM studies on the HN-Ru/RuO$_2$ revealed the complete retention of their original hollow and nanoparticulate structure (Fig. S7 in the ESI†). Furthermore, XPS analysis of the recovered HN-Ru/RuO$_2$
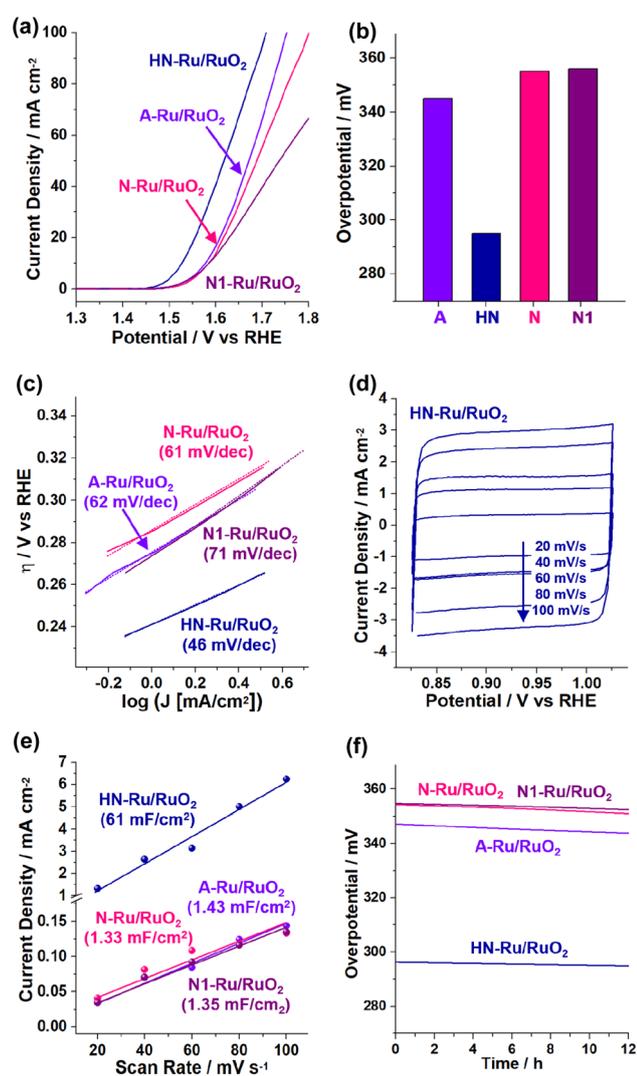
indicated a slight increase in Ru(IV) species from 59% to 64%, accompanied by a slight increase in surface oxygen from 58% to 62% (Fig. S7 in the ESI†). Interestingly, HN-Ru/RuO$_2$ and N1-Ru/RuO$_2$ showed slightly better durability than A-Ru/RuO$_2$ and N-Ru/RuO$_2$, possibly due to the Pd content in the corresponding catalysts.

Recently, various RuO$_2$-based systems have been studied as electrocatalysts for the OER in alkaline electrolytes in the literature.[44-55] Table S2 in the ESI† summarizes the electrocatalytic performance of recent RuO$_2$ materials in alkaline electrolyte (KOH solution) for the OER. For example, RuO$_2$ nanorods and nanoplates have been prepared to show η_{10} values of 320–400 mV and Tafel slopes of 82.5–86 mV dec^{-1}.[44-55] Introduction of additional metal oxides to RuO$_2$ has improved electrocatalytic performance, due to enhanced defects or cooperative catalysis. For example, RuO$_2$/Co$_3$O$_4$ and RuO$_2$/CeO$_2$ nanocomposites have been engineered to show the improved η_{10} values of 302–350 mV and Tafel slopes of 74–74.37 mV dec^{-1}.[44-55] For further improvement of OER performance, additional carbon materials such as carbon nanotubes and doped-graphenes have been incorporated into RuO$_2$, showing η_{10} values of 209–255 mV and Tafel slopes of 56–64 mV dec^{-1}.[44-55] It should be noted that RuO$_2$ nanoparticles without additional carbon materials showed η_{10} values of 302–400 mV and Tafel slopes of 74–86 mV dec^{-1} in the literature (Table S2 in the ESI†). While the η_{10} of 295 mV and the Tafel slope of 46 mV dec^{-1} are not a state-of-the-art world-record, the electrocatalytic performance of HN-Ru/RuO$_2$ is quite inspiring, considering that it resulted from morphology engineering of electrocatalysts. It is also noteworthy that while hollow RuO$_2$ spheres have been engineered, the hollow diameter (61 nm) of HN-Ru/RuO$_2$ is significantly smaller than those (220–660 nm) in the literature.[10,56-59]

Conclusions

Hollow Ru/RuO$_2$ nanoparticles with nanoparticulate shells were engineered using hollow MOPs as templates. Using catechol moieties as anchoring groups, the Ru species could be easily incorporated into hollow MOPs. Heat-treatment of H-MOP-Ru under air resulted in the formation of hollow Ru/RuO$_2$ nanoparticles with nanoparticulate shells. While the diameter of hollow Ru/RuO$_2$ was measured to be 61 nm, the shells of HN-Ru/RuO$_2$ consisted of 6–7 nm nanoparticles. Due to its hollow structure and nanoparticulate shells, HN-Ru/RuO$_2$ showed a high surface area of 80 m^2 g^{-1} and porosity, resulting in superior electrocatalytic performance for the OER to control Ru/RuO$_2$ nanoparticles. We believe that while HN-Ru/RuO$_2$ can be utilized as an HER electrocatalyst[60-62] (Fig. S8 in the ESI†), the H-MOP with catechol moieties in this work can be further applied for the development of electrocatalytic systems for the OER or HER through exploring various metal species.

Author contributions

S. U. Son: conceptualization, supervision, writing the original draft, and review and editing. Y. Myung: supervision, investigation, and formal synthesis. K. Cho, J. Y. Jang, and Y.-J. Ko: investigation and formal analysis.

Conflicts of interest

There are no conflicts to declare.

Acknowledgements

Notes and references

1 K. Kohse-Höinghaus, *Chem. Rev.*, 2023, **123**, 5139–5219.
2 Z. Abdin, N. A. Khafaf, B. McGrath, K. Catchpole and E. Gray, *Sustainable Energy Fuels*, 2023, **7**, 2042–2062.
3 (*a*) B. You and Y. Sun, *Acc. Chem. Res.*, 2018, **51**, 1571–1580; (*b*) Y. Kang, O. Cretu, J. Kikkawa, K. Kimoto, H. Nara, A. S. Nugraha, H. Kawamoto, M. Eguchi, T. Liao, Z. Sun, T. Asahi and Y. Yamauchi, *Nat. Commun.*, 2023, **14**, 4182; (*c*) H. Zhang, W. Wang, Z. Dai, Y. Zhu, M. Cheng, B. Zhang, Y. Feng, Y. Zhang and G. Zhang, *J. Mater. Chem. A*, 2023, **11**, 14674–14681.
4 (*a*) J. Jayabharathi, B. Karthikeyan, B. Vishunu and S. Sriram, *Phys. Chem. Chem. Phys.*, 2023, **25**, 8992–9019; (*b*) Y. Li, W. Wang, M. Cheng, Y. Feng, X. Han, Q. Qian, Y. Zhu and G. Zhang, *Adv. Mater.*, 2023, **35**, 2206351; (*c*) Y. Kang, Y. Guo, J. Zhao, B. Jiang, J. Guo, Y. Tang, H. Li, V. Malgras, M. A. Amin, H. Nara, Y. Sugahara, Y. Yamauchi and T. Asahi, *Small*, 2022, **18**, 2203411; (*d*) Q. Qian, Y. Li, Y. Liu and G. Zhang, *Appl. Catal., B*, 2020, **266**, 118642; (*e*) Q. Qian, Y. Li, Y. Liu, L. Yu and G. Zhang, *Adv. Mater.*, 2019, **31**, 1901139.
5 H. Sun and W. Jung, *J. Mater. Chem. A*, 2021, **9**, 15506–15521.
6 C. Wang, L. Jin, H. Shang, H. Xu, Y. Shiraishi and Y. Du, *Chin. Chem. Lett.*, 2021, **32**, 2108–2116.
7 Y. Li, Y. Wu, T. Li, M. Lu, Y. Chen, Y. Cui, J. Gao and G. Qian, *Carbon Energy*, 2023, **5**, e265.
8 X. Cao, J. Huo, L. Li, J. Qu, Y. Zhao, W. Chen, C. Liu, H. Liu and G. Wang, *Adv. Energy Mater.*, 2022, **12**, 2202119.
9 G. Prieto, H. Tüysüz, N. Duyckaerts, J. Knossalla and G.-H. Wang, *Chem. Rev.*, 2016, **116**, 14056–14119.
10 F. Li, D.-M. Tang, T. Zhang, K. Liao, P. He, D. Golberg, A. Yamada and H. Zhou, *Adv. Energy Mater.*, 2015, **5**, 1500294.
11 W. Zhang, H. Zuo, Z. Cheng, Y. Shi, Z. Guo, N. Meng, A. Thomas and Y. Liao, *Adv. Mater.*, 2022, **34**, 2104952.
12 K. Amin, N. Ashraf, L. Mao, C. F. J. Faul and Z. Wei, *Nano Energy*, 2021, **85**, 105958.
13 M. Khakbaz, A. Ghaemi and G. M. M. Sadeghi, *Polym. Chem.*, 2021, **12**, 6962–6997.
14 J.-S. M. Lee and A. I. Cooper, *Chem. Rev.*, 2020, **120**, 2171–2214.
15 S. Kramer, N. R. Bennedsen and S. Kegnæs, *ACS Catal.*, 2018, **8**, 6961–6982.
16 M. H. Weston, G. W. Peterson, M. A. Browe, P. Jones, O. K. Farha, J. T. Hupp and S. T. Nguyen, *Chem. Commun.*, 2013, **49**, 2995–2997.

17 K. K. Tanabe, N. A. Siladke, E. M. Broderick, T. Kobayashi, J. F. Goldston, M. H. Weston, O. K. Farha, J. T. Hupp, M. Pruski, E. A. Mader, M. J. A. Johnson and S. T. Nguyen, *Chem. Sci.*, 2013, **4**, 2483–2489.

18 S. J. Kraft, R. H. Sánchez and A. S. Hock, *ACS Catal.*, 2013, **3**, 826–830.

19 R. K. Totten, M. H. Weston, J. T. Park, O. K. Farha and J. T. Hupp, *ACS Catal.*, 2013, **3**, 1454–1459.

20 S. J. Kraft, B. Hu, G. Zhang, J. T. Miller and A. S. Hock, *Eur. J. Inorg. Chem.*, 2013, **2013**, 3972–3977.

21 K. K. Tanabe, M. S. Ferrandon, N. A. Siladke, S. J. Kraft, G. Zhang, J. Niklas, O. G. Poluektov, S. J. Lopykinski, E. E. Bunel, T. R. Krause, J. T. Miller, A. S. Hock and S. T. Nguyen, *Angew. Chem., Int. Ed.*, 2014, **53**, 12055–12058.

22 M. H. Weston, Y. J. Colon, Y.-S. Bae, S. J. Garibay, R. Q. Snurr, O. K. Farha, J. T. Hupp and S. T. Nguyen, *J. Mater. Chem. A*, 2014, **2**, 299–302.

23 S. J. Kraft, G. Zhang, D. Childers, F. Dogan, J. T. Miller, S. T. Nguyen and A. S. Hock, *Organometallics*, 2014, **33**, 2517–2522.

24 J. Camacho-Bunquin, N. A. Siladke, G. Zhang, J. Niklas, O. G. Poluektov, S. T. Nguyen, J. T. Miller and A. S. Hock, *Organometallics*, 2015, **34**, 947–952.

25 J. Camacho-Bunquin, M. Ferrandon, U. Das, F. Dogan, C. Liu, C. Larsen, A. E. Platero-Prats, L. A. Curtiss, A. S. Hock, J. T. Miller, S. T. Nguyen, C. L. Marshall, M. Delferro and P. C. Stair, *ACS Catal.*, 2017, **7**, 689–694.

26 K. Cho, S. M. Lee, H. J. Kim, Y.-J. Ko, E. J. Kang and S. U. Son, *Chem.–Eur. J.*, 2020, **26**, 788–794.

27 K. Cho, C. W. Kang, S. H. Ryu, J. Y. Jang and S. U. Son, *J. Mater. Chem. A*, 2022, **10**, 6950–6964.

28 J. Y. Jang, G. H. Kim, Y.-J. Ko, K. C. Ko and S. U. Son, *Polym. Chem.*, 2023, **14**, 2958–2963.

29 J. Chun, S. Kang, N. Park, E. J. Park, X. Jin, K.-D. Kim, H. O. Seo, S. M. Lee, H. J. Kim, Y. H. Kwon, Y.-K. Park, J. M. Kim, Y. D. Kim and S. U. Son, *J. Am. Chem. Soc.*, 2014, **136**, 6786–6789.

30 Z. Zhu and T. M. Swager, *Org. Lett.*, 2001, **3**, 3471–3474.

31 N. Weibel, A. Blaszczyk, C. von Hänisch, M. Mayor, I. Pobelov, T. Wandlowski, F. Chen and N. Tao, *Eur. J. Org Chem.*, 2008, **2008**, 136–149.

32 W. Stöber, A. Fink and E. Bohn, *J. Colloid Interface Sci.*, 1968, **126**, 62–69.

33 M. H. Weston, O. K. Farha, B. G. Hauser, J. T. Hupp and S. T. Nguyen, *Chem. Mater.*, 2012, **24**, 1292–1296.

34 H. Qian, Q. He, J. Zheng, S. Li and S. Zhang, *Polymer*, 2014, **55**, 550–555.

35 M. Henrion, Y. Mohr, K. Janssens, S. Smolders, A. L. Bugaev, O. A. Usoltsev, E. A. Quadrelli, F. M. Wisser, D. E. De Vos and J. Canivet, *ChemCatChem*, 2022, **14**, e202200649.

36 D. J. Morgan, *Surf. Interface Anal.*, 2015, **47**, 1072–1079.

37 W. Wang, S. Guo, I. Lee, K. Ahmed, J. Zhong, Z. Favors, F. Zaera, M. Ozkan and C. S. Ozkan, *Sci. Rep.*, 2014, **4**, 4452.

38 B. K. Manna, P. Panda, R. Mishra and S. Barman, *Energy Fuels*, 2023, **37**, 5613–5622.

39 B. Qi, L. Di, W. Xu and X. Zhang, *J. Mater. Chem. A*, 2014, **2**, 11885–11890.

40 C. Roy, R. R. Rao, K. A. Stoerzinger, J. Hwang, J. Rossmeisl, I. Chorkendorff, Y. Shao-Horn and I. E. L. Stephens, *ACS Energy Lett.*, 2018, **3**, 2045–2051.

41 S. Cherevko, S. Geiger, O. Kasian, N. Kulyk, J. P. Grote, A. Savan, B. R. Shrestha, S. Merzlikin, B. Breitbach, A. Ludwig and K. J. J. Mayrhofer, *Catal. Today*, 2016, **262**, 170–180.

42 T. P. Luxton, M. J. Eick and K. G. Scheckel, *J. Colloid Interface Sci.*, 2011, **359**, 30–39.

43 A. Raveendran, M. Chandran and R. A. Dhanusuraman, *RSC Adv.*, 2023, **13**, 3843–3876.

44 K. Xie, W. Xia, J. Masa, F. Yang, P. Weide, W. Schuhmann and M. Muhler, *J. Energy Chem.*, 2016, **25**, 282–288.

45 H.-S. Park, E. Seo, J. Yang, Y. Lee, B.-S. Kim and H.-K. Song, *Sci. Rep.*, 2017, **7**, 7150.

46 C.-Z. Yuan, Y.-F. Jiang, Z.-W. Zhao, S.-J. Zhao, X. Zhou, T.-Y. Cheang and A.-W. Xu, *ACS Sustainable Chem. Eng.*, 2018, **6**, 11529–11535.

47 R. Jiang, D. T. Tran, J. Li and D. Chu, *Energy Environ. Mater.*, 2019, **2**, 201–208.

48 H.-S. Park, J. Yang, M. K. Cho, Y. Lee, S. Cho, S.-D. Yim, B.-S. Kim, J. H. Jang and H.-K. Song, *Nano Energy*, 2019, **55**, 49–58.

49 M. Zhang, J. Chen, H. Li, P. Cai, Y. Li and Z. Wen, *Nano Energy*, 2019, **61**, 576–583.

50 S. M. Galani, A. Mondal, D. N. Srivastava and A. B. Panda, *Int. J. Hydrogen Energy*, 2020, **45**, 18635–18644.

51 Z. Fan, F. Liao, H. Shi, Y. Liu, M. Shao and Z. Kang, *Inorg. Chem. Front.*, 2020, **7**, 2188–2194.

52 X. Gao, J. Chen, X. Sun, B. Wu, B. Li, Z. Ning, J. Li and N. Wang, *ACS Appl. Nano Mater.*, 2020, **3**, 12269–12277.

53 T. Yu, G. Xu, G. Qian, J. Chen, H. Zhang, L. Luo and S. Yin, *ACS Sustainable Chem. Eng.*, 2020, **8**, 17520–17526.

54 B.-Y. Guo, X.-Y. Zhang, X. Ma, T.-S. Chen, Y. Chen, M.-L. Wen, J.-F. Qin, J. Nan, Y.-M. Chai and B. Dong, *Int. J. Hydrogen Energy*, 2020, **45**, 9575–9582.

55 S. Sarkar, D. Mukherjee, R. Harini and G. Nagaraju, *J. Mater. Sci.*, 2022, **57**, 7680–7693.

56 Z. Peng, X. Liu, H. Meng, Z. Li, B. Li, Z. Liu and S. Liu, *ACS Appl. Mater. Interfaces*, 2017, **9**, 4577–4586.

57 H. Kwon, D. Hong, I. Ryu and S. Yim, *ACS Appl. Mater. Interfaces*, 2017, **9**, 7412–7423.

58 W.-J. Lee, Y.-G. Chun, S.-J. Jang, S.-M. Paek and J.-M. Oh, *J. Alloys Compd.*, 2017, **711**, 611–616.

59 X. Wu, Y. Zeng, H. Gao, J. Su, J. Liu and Z. Zhu, *J. Mater. Chem. A*, 2013, **1**, 469–472.

60 J. Zhang, X. Mao, S. Wang, L. Liang, M. Cao, L. Wang, G. Li, Y. Xu and X. Huang, *Angew. Chem., Int. Ed.*, 2022, **61**, e202116867.

61 Q. Lu, A.-L. Wang, H. Cheng, Y. Gong, Q. Yun, N. Yang, B. Li, B. Chen, Q. Zhang, Y. Zong, L. Gu and H. Zhang, *Small*, 2018, **14**, 1801090.

62 W. Li, Y. Liu, M. Wu, X. Feng, S. A. T. Redfern, Y. Shang, X. Yong, T. Feng, K. Wu, Z. Liu, B. Li, Z. Chen, J. S. Tse, S. Lu and B. Yang, *Adv. Mater.*, 2018, **30**, 1800676.